Infrared Tomographic System for Monitoring the Two-Dimensional Distribution of Atmospheric Pollution over Limited Areas

Fabrizio Cuccoli, Luca Facheris, Simone Tanelli, *Student Member, IEEE*, and Dino Giuli, *Senior Member, IEEE*

***Abstract*—In this paper, we analyze the feasibility and performance of a particular tomographic system for atmospheric pollution monitoring over limited areas (e.g. urban areas). Such a system exploits attenuation-based infrared measurements of the average concentration of the fundamental molecular species of pollutants along rectilinear paths. First, the paper demonstrates the feasibility of an apparatus based on semiconductor infrared laser diode transmitters and passive retroreflectors, capable of measuring the average concentration of pollutants along rectilinear paths with 2 km maximum length, by exploiting their infrared absorption properties. For each gaseous species of interest, the optimal wavelength is then singled out, with the purpose of applying the derivative method for measuring the corresponding average atmospheric concentration. The optimal wavelengths are determined based on both absorption data of atmospheric components and plausible ranges of variation of their concentration. Finally, we present simulations carried out to evaluate the reconstruction of spatial concentration fields of several air pollutants, obtained through a tomographic inversion algorithm exploiting simultaneous attenuation measurements made along different infrared links. Two different network topologies for such measurements are considered.**

***Index Terms*—Diode laser, pollution, semiconductor, tomography.**

I. Introduction

RECENT years have been characterized by a growing interest in systems purposely conceived for measuring urban air pollution. This has been stimulated by the need for detecting, and possibly reducing, the risk of atmospheric pollution in urban areas.

In those cities where atmospheric pollution monitoring systems are active, these are typically based on several spot sensors spread over the urban territory. Exploiting the information provided by these systems, public administrations often take countermeasures to limit emissions that generate atmospheric pollution. On the other hand, data collected by such spot sensors are not sufficient to provide reliable and comprehensive information on diffusion and circulation of pollutants. In fact, the space-time variability of all the phenomena causing air pollution of urban areas depends on several factors (e.g., type, location, and nonstationarity of the pollution sources, meteorological conditions, surrounding orography, etc.) relevant to the aforementioned purpose.

In this paper, we present the feasibility study of a measurement system for continuous monitoring of the spatial concentration of the most common atmospheric pollutants. Such a system performs a number of simultaneous measurements of the mean concentrations of pollutants, based on infrared attenuation measurements along rectilinear paths crossing the area to be monitored, according to a pre-set network topology. These measurements are then given as input to a tomographic processing algorithm to retrieve the two-dimensional (2-D) distribution of concentration of target pollutants in that area. The effectiveness of the system mainly depends on both the feasibility of accurate attenuation measurements through *ad-hoc* infrared transmitter–receiver links spread over the sized target area, and the efficiency of both the network topology and the processing technique for tomographic reconstruction.

Concerning the first issue, in the 1980's, several studies were dedicated to the problem of measuring the mean concentrations along a rectilinear path of the principal molecular species in the atmosphere, exploiting the absorption of infrared electromagnetic radiation by such molecules, were they considered pollutants or not. According to these studies, good results could be achieved by means of small semiconductor diode lasers [1], [2] and a derivative method for spectral measurement. For this reason, in the feasibility study carried out in this paper, we focus on an apparatus based essentially on three instrumental parts, all working at infrared (a lead–salt laser source, a passive retroreflector, and a receiver) and applying the derivative spectral measurement method.

As far as the tomographic reconstruction issue is concerned, solutions were proposed for systems operating at microwaves for measuring space distribution of rainfall [3], [4]. In particular, in [4], an efficient tomographic inversion algorithm is proposed that appears directly exploitable for the system analyzed in this paper as well.

The paper is structured in three parts, corresponding to each of the above topics. In the first part, the basic aspects of the radiation–matter interaction are briefly recalled, together with the principal relationships that can be exploited to determine the mean concentration of the gaseous species along a rectilinear path through infrared attenuation measurements. The second part is the system feasibility study. The basic instrumentation for attenuation measurements is considered that ensures a given accuracy of the spectral measurements needed to determine the mean concentration of gaseous species along a rectilinear

Manuscript received September 24, 1998; revised March 1, 1999. This work was supported by the Italian Ministry for University and Scientific/Technological Research.

The authors are with the Dipartimento di Ingegneria Elettronica, Università di Firenze, Firenze, Italy (e-mail: facheris@ingfi1.ing.unifi.it).

Publisher Item Identifier S 0196-2892(00)05150-0.

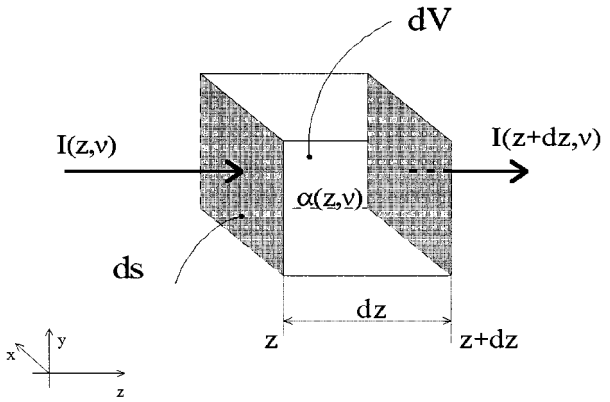

Fig. 1. Power spectral density per unit area and propogation coordinates.

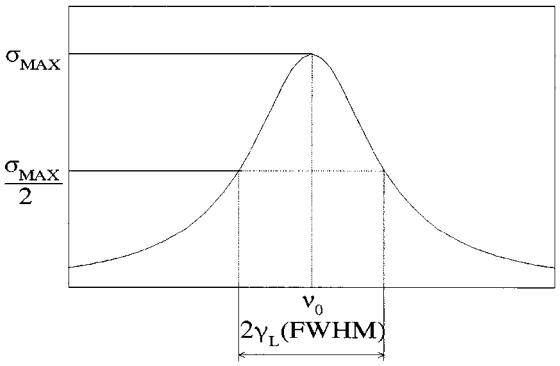

Fig. 2. Lorentzian shape of the absorption section (versus wavenumber).

path with a maximum length of at least of 2 km. The problem of finding the optimal emission wavelength for the molecular species of interest is jointly analyzed, so that the derivative method [5] could be used for measuring the average concentration. The reported results were obtained using the absorption parameters provided by the Hitran database [6] [7], adopted referring to carbon monoxide, nitrogen oxide, and ozone. The third part is devoted to the application of the tomographic inversion algorithm adopted for the retrieval of simulated fields of concentration. In particular, we report the results of the reconstruction of carbon monoxide concentration fields as generated by a point source. The considered concentration fields have been generated through simple mathematical models for atmospheric diffusion. Two different measurement networks topologies, consisting of crossed rectilinear paths, were used in simulations carried out to evaluate the performance of the tomographic system.

II. Attenuation of Infrared Radiation in the Atmosphere

The basic task of the measurement system discussed in this paper is to measure the average concentration of molecular species by exploiting their infrared radiation absorption properties. The basic Lambert–Beer law describes well the behavior of an electromagnetic wave with wavenumber ν (the inverse of the wavelength) that propagates in the atmosphere [8], [9]

$$\frac{dI(\nu, z)}{dz} = -\alpha(\nu, z) \cdot I(\nu, z) \tag{1}$$

where $I(z, \nu)$ is the power spectral density per unit area (in Watt/cm^2@Hz) at distance z along the wave propagation axis (see Fig. 1), and $\alpha(z, \nu)$ (in cm^{-1}) is the attenuation coefficient.

The attenuation coefficient can be expressed as the sum of three terms

$$\alpha = \alpha_R + \alpha_M + \alpha_G \tag{2}$$

where α_R and α_M account for attenuation due to Rayleigh effect (i.e. diffusion of the incident radiation by atoms and molecules), and to Mie effect (diffusion by particles and aerosols with size comparable to the wavelength), respectively, while α_G accounts for attenuation due to molecular absorption. α_G can be further decomposed, accounting for the contribution of each molecular species. In the case of horizontal short-range paths of propagation, the absorption section can be assumed as independent of z. Therefore, α_G can be written as

$$\alpha_G(\nu, z) = \sum_{i=1}^{N} \sigma_{G,i}(\nu) \cdot N_i(z) \tag{3}$$

where $\sigma_{G,i}$ (cm^2) and N_i (molecules per cm^3) are respectively the absorption section and the concentration of the ith molecular species.

Molecular absorption is due to transitions between vibration–rotation states that are peculiar to each molecular species. The generic absorption section $\sigma_{G,i}(\nu)$ is characterized by a regularly continuous variation with wavelength, that depends on pressure and temperature, too. The functional shape of the absorption section versus wavelength depends on Doppler and collisional effects. In standard atmosphere conditions (1 atm and 25°C), collisional effects dominate, and the absorption section due to a generic single spectral absorption line j, of a generic molecular specie i, takes on the typical Lorentzian form [5] sketched in Fig. 2:

$$\sigma_{G,ij}(\nu) = \frac{S_{ij}}{\pi} \cdot \frac{\gamma_{L,ij}}{(\nu - \nu_{0,ij})^2 + \gamma_{L,ij}^2} \tag{4}$$

where $\nu_{0,ij}$ and L,ij are the center line wavenumber and width, respectively (both expressed in cm^{-1}), and S_{ij} is the line strength (in cm/molecule).

In the wavelength interval 1–20 μm, α_G varies with wavelength much more than α_R and α_M. This behavior is exploited to measure the concentration of molecular species by means of the derivative method [5], [8] described in the next section.

III. Attenuation Measurement Method

Consider the measurement scheme sketched in Fig. 3. Suppose that the transmitter is emitting a continuous monochromatic radiation with spectral incidence power $I_o(\nu)$. Then the spectral incidence power $I_r(\nu)$ at the receiver (supposed located at distance L) is obtained by integrating (1)

$$I_r(\nu) = I_0(\nu) \cdot \exp\left[-\int_0^L \alpha(\nu, z)\, dz\right]. \tag{5}$$

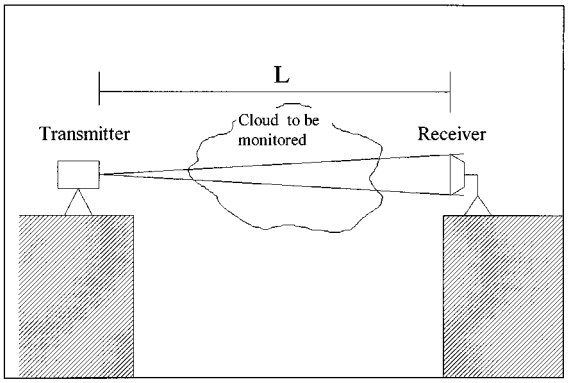

Fig. 3. Transmitter–receiver measurement scheme.

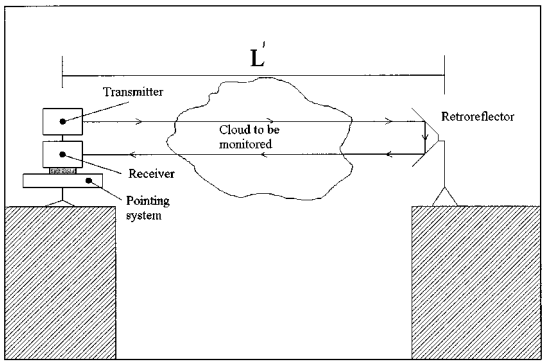

Fig. 4. Measurement scheme with passive retroreflectors.

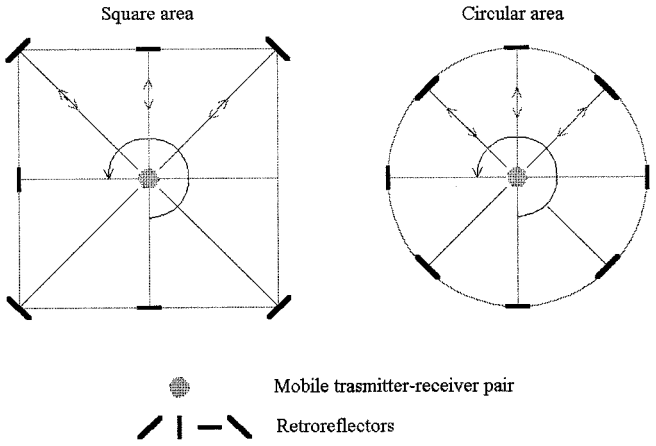

Fig. 5. Two measurement networks using one transmitter–receiver pair.

Correspondingly, the power spectral density $P_r(\nu)$ actually sensed by the receiver is given by

$$P_r(\nu) = KP_{T0}(\nu) \cdot \exp\left[-\int_0^L \alpha(\nu, z)\, dz\right] \tag{6}$$

where $P_{T0}(\nu)$ is the transmitted power density, and K is the optical efficiency accounting for all optical losses of the system.

Equation (6) can be rewritten as

$$P_r(\nu) = KP_{T0}(\nu) \cdot \exp\left\{-\left[\overline{N}_m L\sigma_m(\nu) + \gamma(\nu)\right]\right\} \tag{7}$$

where $\sigma_m(\nu)$ and $\overline{N}_m$are, respectively, the absorption section and the average concentration of the species of interest along the path of length L, and γ expresses all the other attenuation contributions.

Under the hypothesis that both the optical efficiency K and the transmitted power P_{T0} are independent of the wavenumber, the ratio between the derivative of (7) (made with respect to ν) and (7) itself provides

$$S(\nu) \equiv \frac{1}{P_r(\nu)} \frac{dP_r(\nu)}{d\nu} = -\left[\overline{N}_m L \frac{d\sigma_m(\nu)}{d\nu} + \frac{d\gamma(\nu)}{d\nu}\right] \tag{8}$$

where $S(\nu)$ is referred to as "spectral sensitivity of the received power."

When the second term in (8) is negligible with respect to the first one, $S(\nu)$ is proportional to the average concentration

$$S(\nu) = -\overline{N}_m L \frac{d\sigma_m(\nu)}{d\nu}. \tag{9}$$

Assuming that $\sigma_m(\nu)$ is known, $\overline{N}_m$ can then be estimated from (9). The assumption made to obtain (9) is valid only in some wavenumber intervals. It is therefore of particular interest to single out, for each species of interest, the wavenumber intervals where (9) can be exploited without introducing excessive approximations. This issue is discussed in Section V. The instrument described in the next section is designed to directly measure $S(\nu)$ in order to estimate $\overline{N}_m$ by inverting (9).

IV. The Instrument for Attenuation Measurement

The main devices that can be used to build up the proposed apparatus for measuring attenuation along a direct transmitter–receiver link or transmitter-passive retroreflector–receiver link are the following:

infrared semiconductor diode laser (SDL);
hollow corner cube retroreflector;
infrared receiver;
optical devices for collimating and collecting infrared power;
electronic and control devices.

The average concentration measurement is performed by assembling such devices according to the scheme of Fig. 4. The use of passive retroreflectors and of step scanning platforms makes it possible to cover an area with several links and one single transmitter–receiver pair. Two possible path geometries are shown in Fig. 5.

The main reasons for utilizing SDL's as transmitters of infrared radiation are the following.

1) The emission line width (about 1 MHz), is small enough to resolve the spectral shape of $\sigma_m(\nu)$ (the width of the absorption section contributed by one single absorption line is of the order of 30–300 MHz) [1], [2], [5].
2) The emission power under mono-modal propagation (at least 100 μW), allows measurements of average concentrations up to about 2 km transmitter–receiver distance, as shown in Section IV.
3) The possibility of varying the emission frequency of the SDL by means of the supply current allows the measurement of the derivative of the received power, as needed to

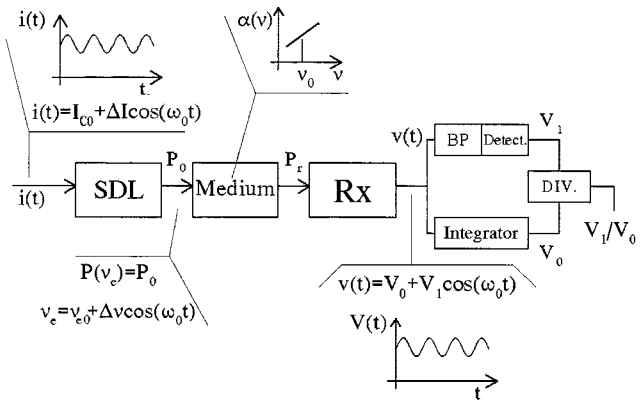

Fig. 6. System configuration exploitable for measurements.

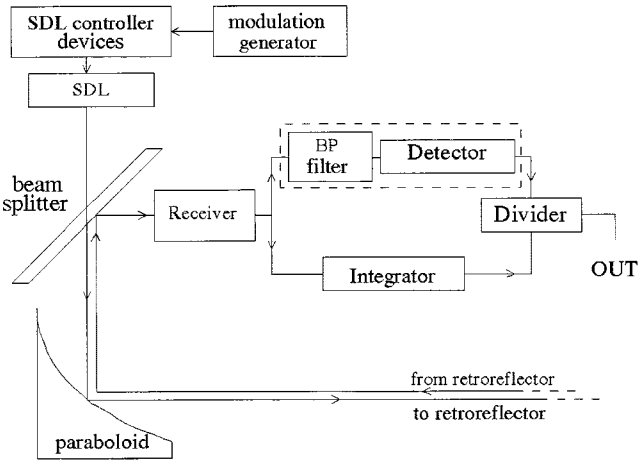

Fig. 7. Arrangement of the devices on mobile aiming system.

measure the average concentration through the derivative method.

$S(\nu)$ can be measured by means of the instrument sketched in Fig. 6. The following assumptions are made.

1) Within the modulation interval of the SDL supply current, the emitted power P_{T0} can be considered as independent of the emission frequency.
2) The emission frequency ν_e (in wavenumber) of the SDL is equal to ν_{eo} when the supply provides a constant current I_{co}.
3) The supply current is amplitude modulated (modulation amplitude ΔI) with a sinusoidal waveform with frequency ω_o. Thus, the SDL emission frequency ν_e is modulated analogously, with modulation amplitude $\Delta\nu$);
4) the absorption coefficient $\alpha(\nu)$ changes linearly in the frequency interval $[-\Delta\nu, \Delta\nu]$.

The SDL parameters values utilized in this feasibility study are taken from commercial data sheets and are in good agreement with those reported in [10]. Under such assumptions, the DC component V_o of the receiver output is proportional to the power received in the absence of modulation, while the amplitude of the first harmonic V_1 is proportional to the derivative of the received power. Thus, one gets the following proportionality relationship

$$S(\nu)_{\nu_{eo}} \propto \frac{V_1}{V_0} \tag{10}$$

and, from (9):

$$\overline{N}_m \propto \frac{V_1}{V_0} \tag{11}$$

Fig. 7 shows a possible arrangement of the devices on the scanning platform. The beam splitter is needed to separate the transmitted laser beam from the received one. The paraboloid, with an off-axis focus, serves as collimating mirror both from and toward the corner-cube retroreflector.

V. Measurable Attenuation

A basic problem of the feasibility study concerning attenuation measurements through a generic infrared transmitter–receiver link of given length is to verify whether the power collected at the receiver's output can be exploited for attenuation measurements. Still assuming that $\alpha(\nu, z)$ is constant along the propagation coordinate z and assuming the path geometry of Fig. 4, (6) becomes

$$P_r(\nu) = KP_{T0}(\nu) \cdot \exp[-2\alpha_G L'] \cdot \exp[-2\alpha_T L'] \tag{12}$$

where $\alpha_T = \alpha_R + \alpha_M$ and L is the distance between the transmitter and the retroreflector.

For such a reference check, the following parameters were considered, based on the instrument configuration of Fig. 7:

1) laser diode emission characteristics;
2) efficiency of the optical devices (beam splitter, paraboloid and retroreflector);
3) receiver's characteristics.

Based on the above parameters, the objective is to estimate the maximum value of α_G in (12) that still allows the received power to exceed the minimum detectable power at the receiver. For this purpose, plausible values of K and α_T must be estimated, based on the previously listed issues and as discussed in the following.

A. Parameters Influencing the Optical Efficiency

The parameter K can be factorized in five contributing terms as follows:

$$K = \varepsilon_{s1} \cdot \varepsilon_{ts} \cdot \varepsilon_{rr} \cdot \varepsilon_{rx} \cdot \varepsilon_{s2} \tag{13}$$

where

ε_{s1} efficiency of beam splitter in transmission;
ε_{ts} efficiency of the paraboloid in transmission;
ε_{rr} efficiency of the retroreflector;
ε_{rx} efficiency of the paraboloid in reception;
ε_{s2} efficiency of beam splitter in reception.

The three efficiencies ε_{s1}, ε_{s2}, and ε_{ts} depend on the specific characteristics of the devices and on the relative positions of transmitter, beam splitter, paraboloid, and receiver. Plausible values of each of them range between 0.5 and 1. Instead, the link geometry plays a fundamental role for ε_{rr} and ε_{rx}. In fact, besides depending on the devices' characteristics, they are basically determined by the length of the link and by atmospheric

TABLE I
CONCENTRATION RANGES OF SOME MOLECULES IN THE FLORENCE URBAN ATMOSPHERE

Molecule	min [ppm]	max [ppm]
H_2O	5000	50000
CO_2	400	400
O_3	0.005	0.2
N_2O	0.01	0.012
CO	0.01	10
CH_4	2	2
O_2	209480	209480
NO	0.001	0.3
SO_2	0.0005	0.1
NO_2	0.0005	0.5
NH_3	0.01	0.01
N_2	780840	780840

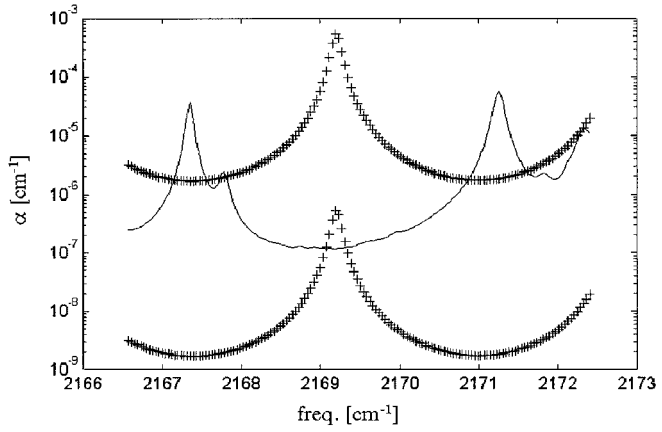

Fig. 8. Attenuation coefficients for carbon monoxide. Upper cross line curve: attenuation coefficient for a 10 ppm CO concentration. Lower cross line curve: attenuation coefficient for a 0.1 ppm CO concentration. Continuous line curve: attenuation coefficient due to all absorbing molecules excepted CO, considering their maximum concentration.

turbulence (laser beam widening and fluctuations of the propagation direction, caused by variations of the air refraction index [11]–[13]). Under the hypothesis of a Gaussian laser beam, the efficiency of the retroreflector is given by

$$\varepsilon_{rr}(l) = \gamma_{rr} \cdot \left(1 - \exp\left(\frac{-d^2}{2w^2(l)}\right)\right) \tag{14}$$

where

- γ_{rr} reflection efficiency of the reflecting surface;
- d the retroreflector diameter;
- $w(l)$ beamwidth at the retroreflector position (at distance l from the emitting source).

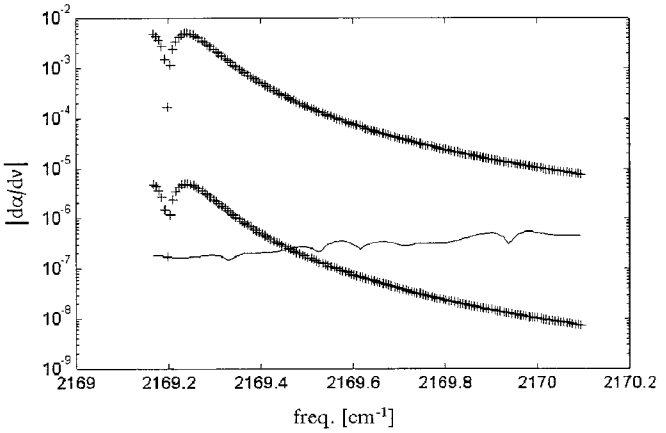

Fig. 9. Derivative of the attenuation coefficient reported in Fig. 8. Notice: only the wavenumber interval of interest is reported.

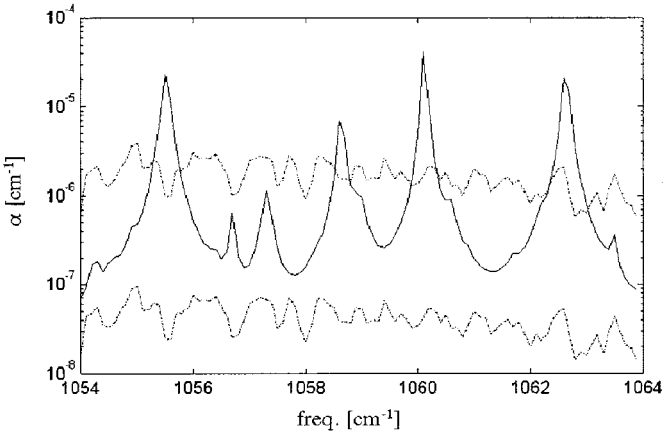

Fig. 10. Attenuation coefficients for ozone. Upper point-line curve: attenuation coefficient for a 0.2 ppm O_3 concentration. Lower point-line curve: attenuation coefficient for a 5 ppb O_3 concentration. Continuous line curve: attenuation coefficient due to all absorbing molecules except O_3, considering their maximum concentration.

In far field conditions and for small beam divergence angle θ, $w(l)$is approximated by $\theta \cdot l$.

In the configuration considered in Fig. 7, the beam divergence angle depends exclusively on the paraboloid angular deviation θ_p. Typical values of $\gamma_{rr} \approx 1, \theta_p = 6$ arc min and $d = 100$ mm (Melles Griot Catalogue) give $\varepsilon_{rr} = 1.65 \cdot 10^{-3}$. ε_{rx} can be estimated through an analogous expression

$$\varepsilon_{rx} = \frac{d_p}{2(d + L\theta_d)} \tag{15}$$

where d is the diameter of the paraboloid, and θ_d is the angular deviation of the retroreflector. For $d_p = 200$ mm and $\theta_d = 30$ arc sec, we get $\varepsilon_{rx} = 0.41$. Based on the aforementioned plausible values of the efficiency coefficients, K can be estimated around 10^{-4}.

For the purposes of following exposition, the effects of turbulence are considered as related to laser beam broadening and laser beam axis wandering.

1) Laser Beam Broadening: The statistical characteristics of laser propagation have been studied and analyzed utilizing

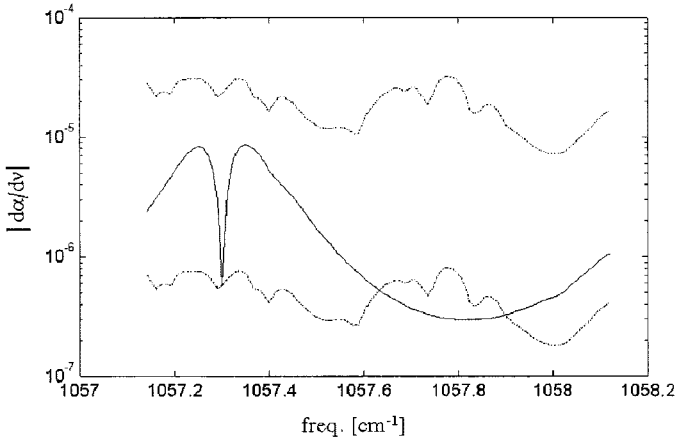

Fig. 11. Derivative of the attenuation coefficient reported in Fig. 10. Notice: only the wavenumber interval of interest is reported.

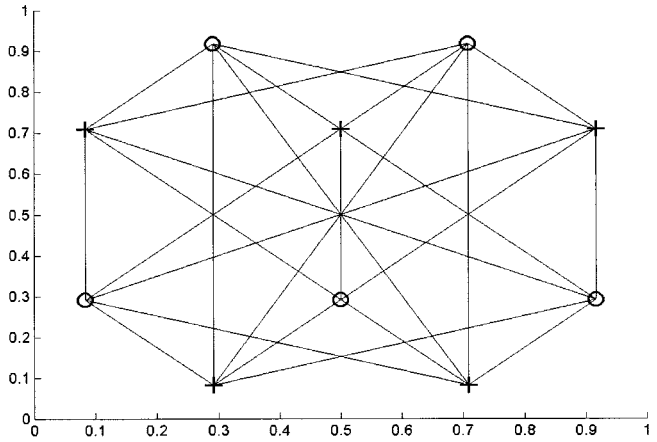

Fig. 12. Measurement network NET01: + transmitter–receiver pair; O retroreflector.

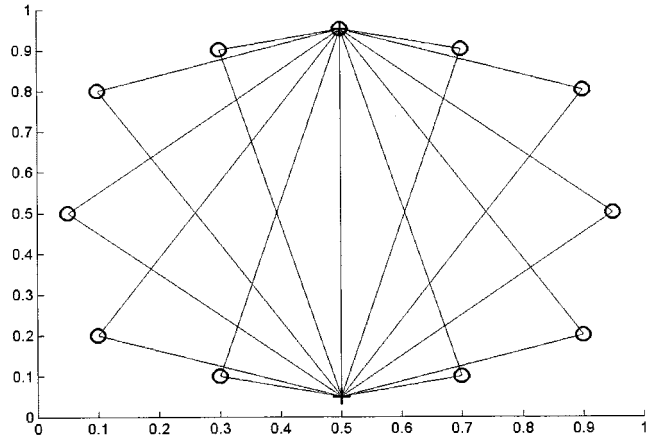

Fig. 13. Measurement network NET02: symbols are the same as in Fig. 12.

the unimodal Gaussian model [11], [12]. Under such assumptions, the mean value of the power surface density can be expressed as follows:

$$\langle I(\rho, z)\rangle = \left|U_o^2\right| \cdot \frac{w_o^2}{\rho_e^2(z)} \cdot \exp\left(-\frac{\rho^2}{\rho_e^2(z)}\right) \tag{16}$$

where

- ρ distance of the generic point in the plane orthogonal to the propagation axis z
- U_o amplitude of the transmitted field;
- w_o beamwidth at $z = 0$;
- $\rho_e(z)$ beamwidth at distance z.

In far field conditions ($z \gg \pi w_o/\lambda$) and for focused radiation, $\rho_e(z)$ becomes

$$\rho_e(z) = \frac{z\lambda}{2\pi w_o}\sqrt{\left(1 + \frac{4w_o^2}{3\rho_o^2}\right)} \tag{17}$$

where ρ_0 is the coherence radius of a plane wave in the turbulent atmosphere given by

$$\rho_o = \left(9.16\frac{r_o^{-5/3}z}{L_o}\right)^{-3/5} \tag{18}$$

where L_o is the length of a propagation path locally parallel to the Earth's surface and r_o is the Fried parameter. Values of r_o in the infrared region were obtained by extrapolating experimental data obtained in the visible region for $L_o = 20$ km [13]. In particular, $r_o = 18.5$ cm for $\lambda = 4$ μm and $r_o = 49$ cm for $\lambda = 9$ μm. Therefore, assuming $w_o = 10$ cm (which is definitely greater than standard values), then at $L_o = 1$ km and for wavelengths less than 10 μm, (17) indicates that turbulence causes a beamwidth increase smaller than the 10% with respect to the absence of turbulence (i.e., $\rho_o \to \infty$).

2) Laser Beam Axis Wandering: This effect is usually described through the fluctuations of the centroid of the surface power density over a plane orthogonal to the ideal propagation direction. Such fluctuations, depending on the variations of atmospheric turbulence, are slowly varying with respect to the variations of the parameters influencing the estimate of $S(\nu)$. Therefore, when estimating the left-hand ratio of (8), expressing the ratio between the spectral power density and its derivative, the axis wandering effects practically cancel each other.

B. Parameters Influencing α_T

The Rayleigh attenuation effects can be obtained from the Rayleigh diffusion cross section $\sigma_R(\nu)$ [14]:

$$\alpha_R = \sigma_R(\nu) \cdot N \tag{19}$$

where N is the number of molecules per unit volume. In the atmospheric layers below 100 km, we have [8]:

$$\sigma_R(\nu) = 456 \cdot 10^{-27}\left[\frac{\nu}{1.82 \cdot 10^4}\right]^4 \tag{20}$$

where ν is the wavenumber expressed in cm^{-1}. The Mie attenuation coefficient, accounting for the attenuation effects due to particles and aerosol, is given by:

$$\alpha_M = \int_0^\infty \sigma_M(a, \lambda, m)N(a)\,da \tag{21}$$

where $\sigma_M(a, \lambda, m)$ is the absorption section expressed as a function of the wavelength λ, of the particle's equivalent

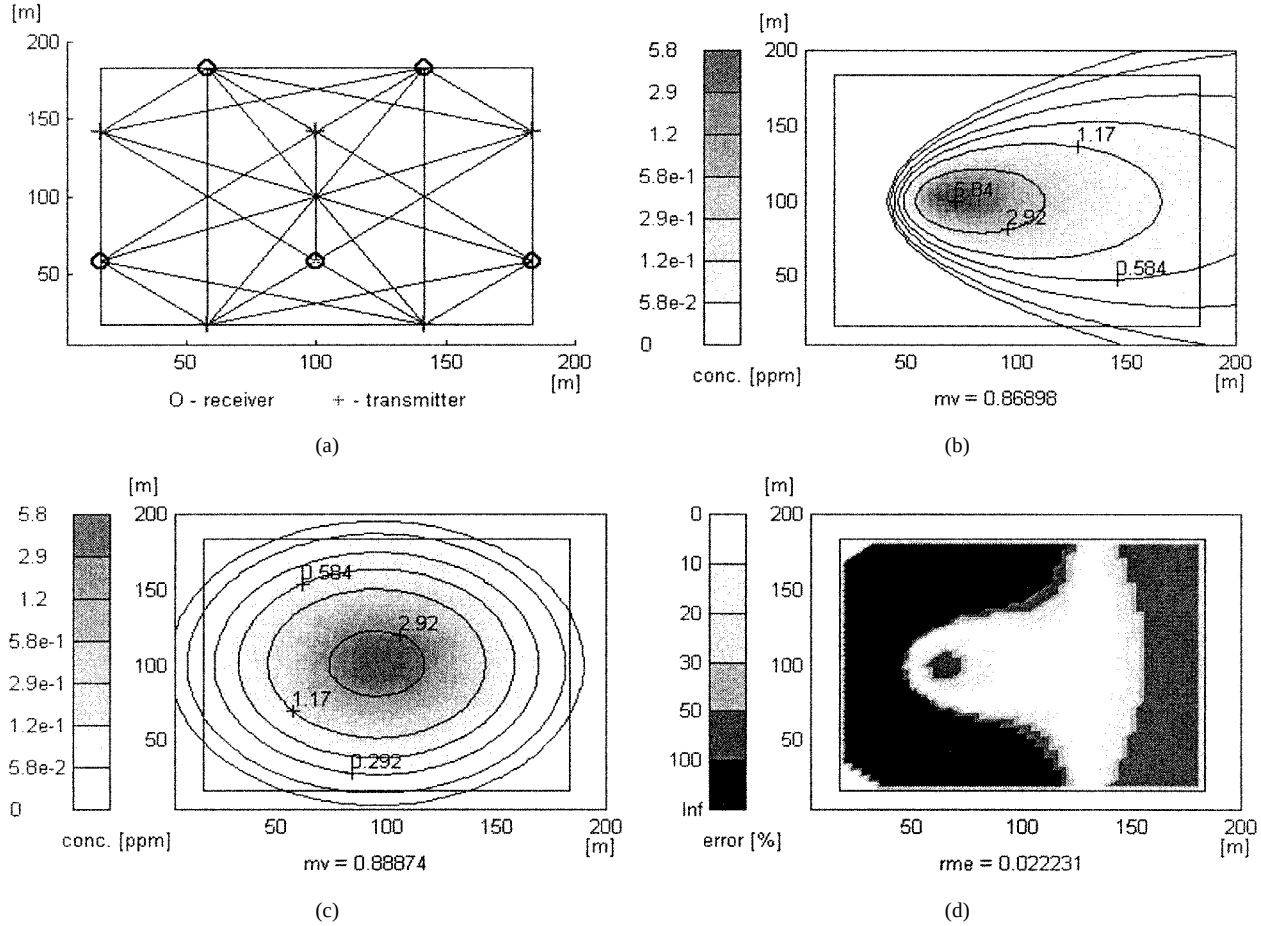

Fig. 14. Reconstruction of the simulated concentration field produced by a CO spot source, Pasquill's stability class A. Wind direction: horizontal. Source position: (20, 100, 0.5) m. (a) The measurement network used (NET01), (b) the simulated concentration field (mv is the average concentration over the area), (c) the reconstructed concentration field (mv as before), and (d) the 2-D distribution of the relative error (rme is the relative error for average concentration).

diameter a and of the refraction index m. $N(a)$ is the volumetric density of the particles with equivalent diameter between a and $a+da$. One of the simplest relationships for $N(a)$ is that by Kruse *et al.* [15]:

$$\alpha_M = \frac{3.91}{R_V} \cdot \left[\frac{\nu}{1.82 \cdot 10^4}\right]^q; \quad \begin{cases} q = 0.585 R_V^{1/3}, & \text{for } R_V \le 6 \text{ km} \\ \approx 1.3, & \text{otherwise} \end{cases} \tag{22}$$

where R_V is the meteorological visual range, expressed in km.

Depending on the visibility conditions, α_M ranges between 10^{-4} and 1 km^{-1}. In our range of interest $\approx 1 \div 10$ μm, the Mie effects prevail. Therefore, for $L = 1$ km, $\exp(-2\alpha_T L')$ ranges between 0.14–1.

C. Minimum Detectable Power at the Receiver

The minimum power that can be detected by the receiver depends mainly on the detectability D, defined as

$$D = \frac{\frac{S}{N}\Delta f^{1/2}}{P_r A^{1/2}} \tag{23}$$

where S/N is the SNR at the receiver's output, Δf is the receiver's noise bandwidth, and A the receiver's active area (in cm^2). Considering $A = 10^{-2}$ cm^2, $\Delta f = 10$ Hz (typical values for available devices), and assuming a minimum acceptable SNR $(S/N)_{\text{MIN}} = 2$ from (23), we get the corresponding minimum acceptable power (in Watts) as a function of D

$$(P_r)_{\text{MIN}} = 0.63 \cdot D^{-1} \tag{24}$$

In the infrared region, D typically ranges between 10^8 and 10^{10} cm Hz$^{1/2}$/W. Thus, $(P_r)_{\text{MIN}}$ ranges between 6.3 nW and 63 pW.

D. Estimating the Variation Interval of α_G

Solving (12) with respect to α_G, we get

$$\alpha_G = -\frac{1}{2L'} \cdot \ln\left(\frac{P_r(\nu)}{K \cdot P_{To} \cdot \exp(-2\alpha_T L')}\right) \tag{25}$$

Substituting to $P_r(\nu)$ the minimum acceptable power $(P_r)_{\text{MIN}}$, we get the maximum molecular absorption coefficient $\alpha_G)_{\text{MAX}}$ that can be measured in the described framework. Under the following hypotheses:

1) $(P_r)_{\text{MIN}} = 63$ pW;

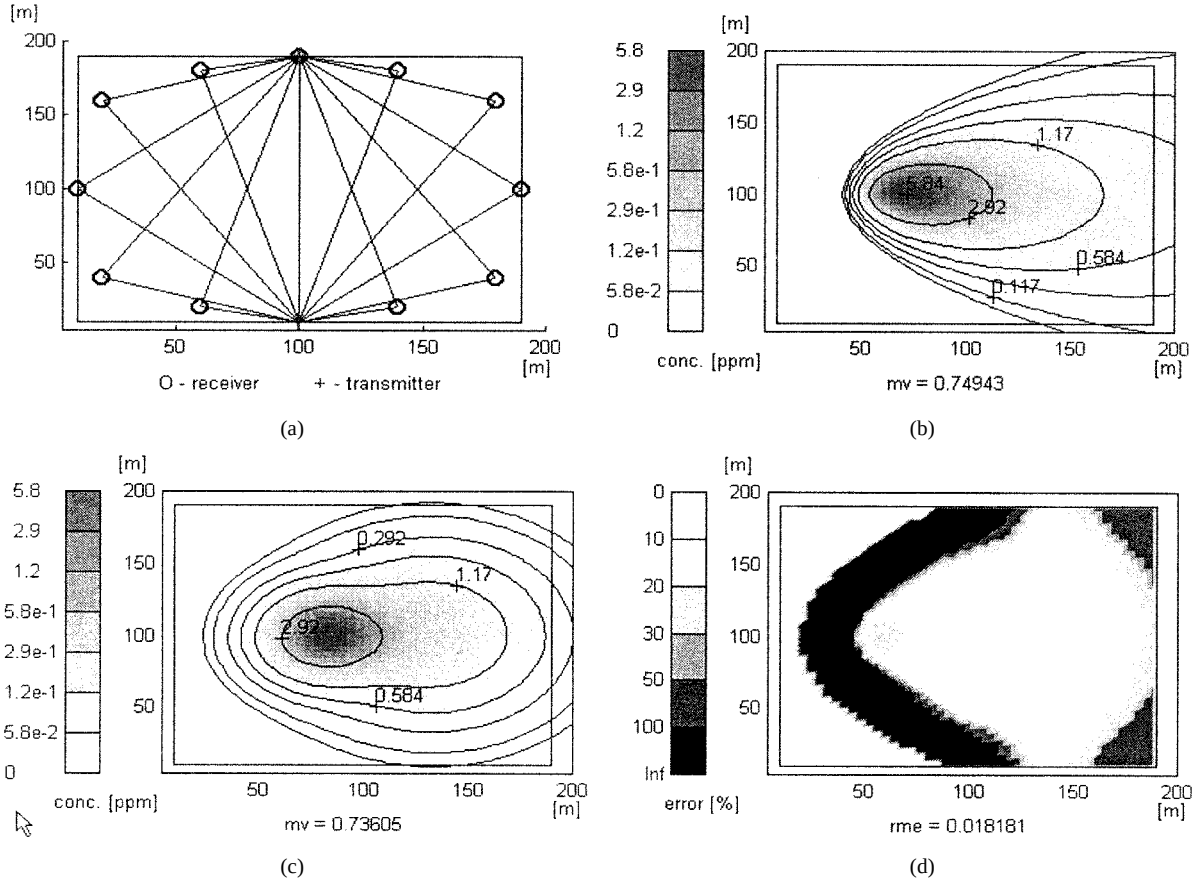

Fig. 15. As Fig. 14, for NET02.

2) $L' = 1$ km;
3) $P_o = 100$ μW (the typical power emitted by a tunable lead–salt SDL);
4) $\exp(-2\alpha_T L') = 10^{-1}$;
5) $K = 10^{-4}$.

we estimated a maximum molecular attenuation coefficient of about $2 \cdot 10^{-5}$ cm^{-1}. Notice that, since α_G depends logarithmically on all parameters involved in (25), exception made for L', variations of some orders of magnitude of such parameters do not influence significantly $(\alpha_G)_{\mathrm{MAX}}$. Therefore, for $L' = 1$ km, $(\alpha_G)_{\mathrm{MAX}} = 10^{-5}$ is a quite realistic limit value exploitable in the search for optimal wavelengths, as discussed in the following Section.

VI. Optimal Wavelengths

As mentioned at the end of Section II, in order to make the system in Fig. 4 profitable for the measurement of $S(\nu)$ defined in (9), it is necessary to single out as many suitable wavelengths as the number of species for which the average concentration measurement must be carried out. The reason is that the derivative of the attenuation coefficient of the species of interest must be at least one order of magnitude greater than the derivative of the attenuation coefficient contributed by all other species that are simultaneously present.

We searched for such optimal wavelengths by exploiting the characteristic parameters of the absorption lines ν_0, γ_L and S and the minimum and maximum expected concentrations of the main molecules that are normally present in the atmosphere. We utilized the HITRAN database version 1986 of the US.AFGL as reference for the absorption lines parameters [6], [7]. The minimum and maximum concentrations in Table I apply to the town of Florence from ground up to 50 m height and were provided by Agenzia Regionale Protezione Ambiente e Territorio (the Regional Agency for Environmental Protection, ARPAT). Notice that for each of them, only the absorption lines of the principal isotopes were considered.

Minimum and maximum concentrations for water were determined assuming the following minimum and maximum values: -5° C and 34° C for temperature, 30% and 100% for relative humidity. Such values correspond to the yearly climatic excursions in the town of Florence.

The basic pollutant molecules for which we singled out the optimal wavelength are CO (carbon monoxide), O_3 (ozone), NO, NO_2, and N_2O (nitrogen oxides).

For carbon monoxide, we got the wavenumber interval 2169.2–2170 cm^{-1} (corresponding to the wavelength interval 4.608–4.609 μm). Concentrations ranging from 0.1–10 ppm can be measured in such intervals. Fig. 9 shows that in that interval, the absolute value of the derivative of the attenuation coefficient due to CO always dominates that contributed by the other species. When concentration is high, the attenuation coefficient becomes of the order of 10^{-4} (see Fig. 8), which could be too great to guarantee an acceptable received

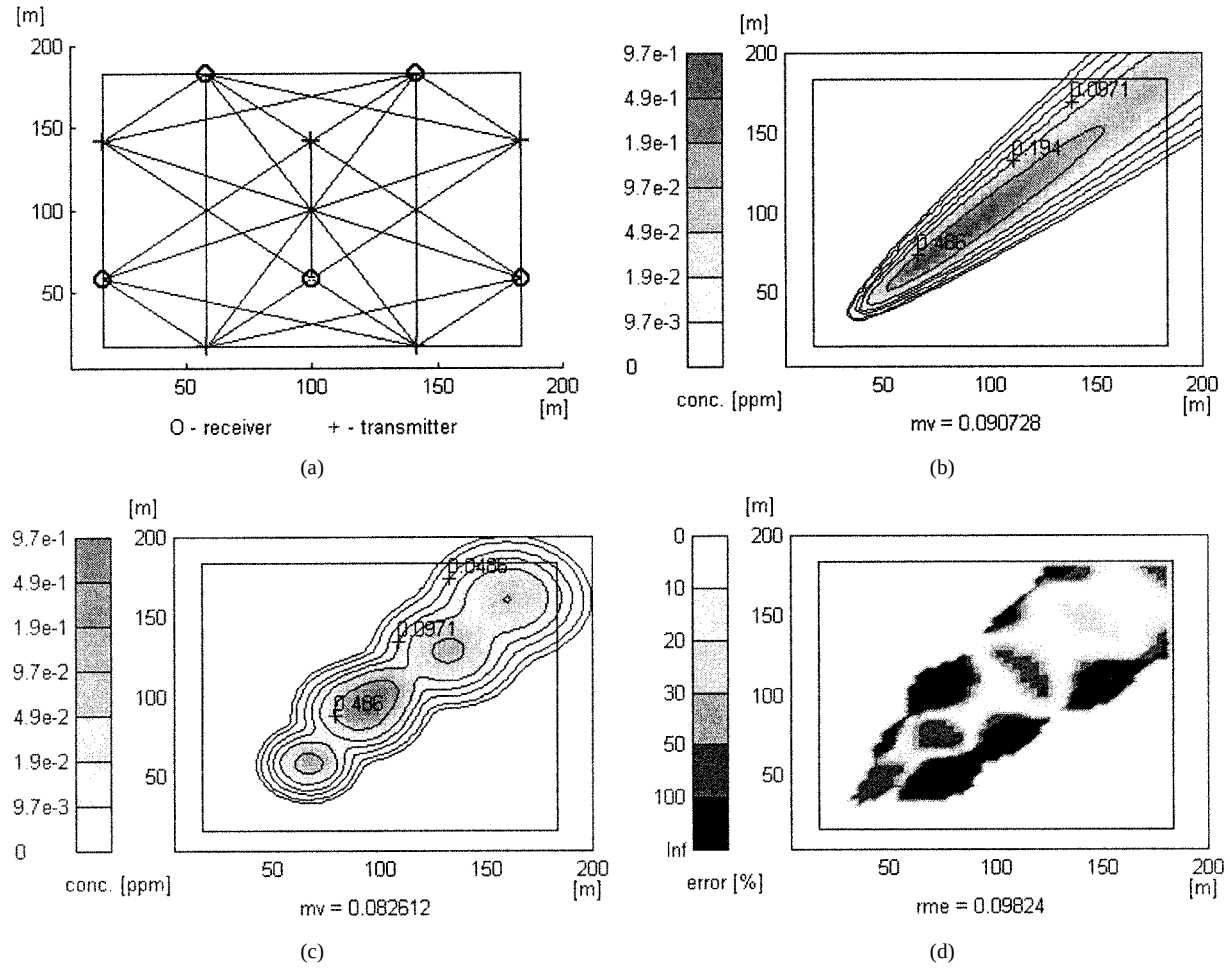

Fig. 16. As Fig. 14, for Pasquill's stability class D. Wind direction: 45° with respect to the horizontal. Source position (20, 20, 0.5) m.

power. Therefore, when the CO concentration gets close to the maximum, it is advisable to utilize wavenumbers greater than 2169.5 cm^{-1}. The results of Fig. 8 and Fig. 9 were obtained by accounting for the contribution of the absorption lines of the principal isotopes of all the molecules listed in Table I, having their center line frequency ν_0 included in the interval 2164–2174 cm^{-1}.

For ozone, an optimal wavenumber of 1057.77 cm^{-1} (9.454 μm) was found in the same manner. Figs. 10 and 11 are obtained accounting for the contribution of lines included between 1052–1064 cm^{-1}. Fig. 11 shows that the 1057.77 cm^{-1} wavenumber is sufficient to measure ozone concentrations ranging between 0.005–0.2 ppm.

For nitrogen oxides, we got the following optimal wavenumbers: 2240.41 cm^{-1} (4.45 μm) for N_2O, 1900.04 cm^{-1} (5.26 μm) for NO, and 843.71 cm^{-1} (11.85 μm) for NO_2.

VII. Tomographic Reconstruction of Concentration Fields and Performance Evaluation

Attenuation measurements made separately and simultaneously along different rectilinear paths, if opportunely processed, can provide the 2-D fields of the concentration of the molecular species of interest. In this section, after a brief introduction of the tomographic reconstruction problem and of the specific solution adopted, we describe the simulation set-up chosen to generate reference 2-D spatial distributions of concentration of air pollutants. Simulation results concerning the performance of the proposed tomographic system for such a simulation set-up are finally presented.

A. Attenuation-Based Tomographic Inversion Algorithm

In principle, simultaneous measurements of attenuation made along different receiver-transmitter paths can be exploited to estimate the 2-D distribution of the physical entity causing such attenuation. When trying to use this principle to monitor that entity over a geographical area, the problems that must be faced are mainly related to the underdetermination generated by the practical and economical impossibility to arrange an adequate number of links over the monitored areas.

In 1991, a first tomography approach of this kind was proposed [3]. There, the objective was to estimate rainfall fields, exploiting attenuation measurements at microwaves made on a set of independent transmitter–receiver links that should be distributed within the area to be monitored, not larger than 400 km^2. 2-D specific attenuation fields at microwaves could be estimated as linear combinations of 2-D basis functions after an iterative, deterministic process that needed some physical constraints to be posed in order to guarantee convergence. Through standard specific attenuation-rainfall relationships, the

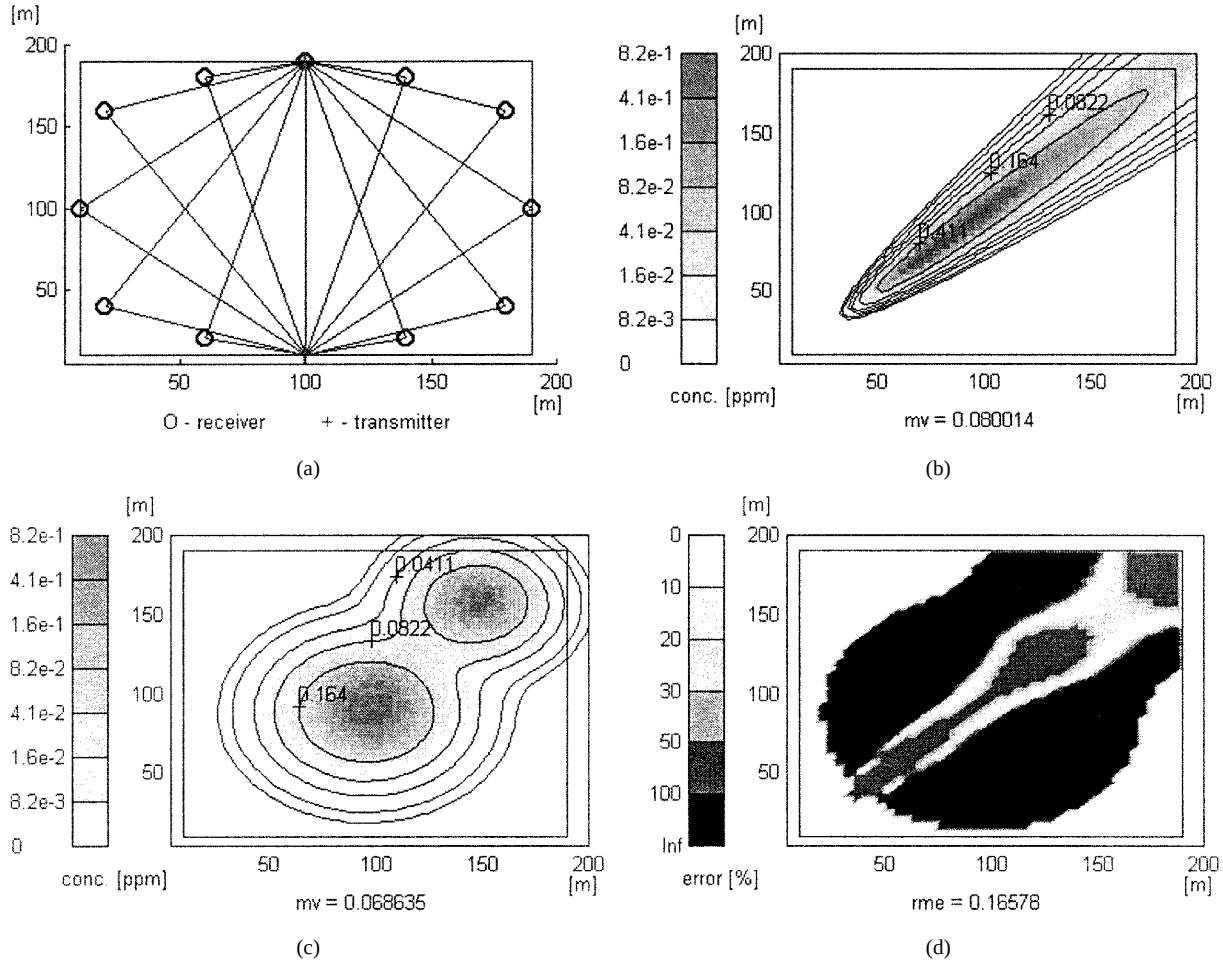

Fig. 17. As Fig. 16, for NET02.

rainfall fields causing that attenuation could then be derived. Since that first proposal, it was envisaged that the special inversion problem to be faced deserved further investigation concerning the optimal choice of the basis functions, the use of adaptive algorithms, and the evaluation of overall system performance. Recently, a more flexible and robust approach to such a problem has been proposed, referred to as stochastic reconstruction technique (SRT), based on an initial stochastic solution search followed by a finite sequence of optimization and control phases [4]. Besides overcoming some problems of the previous tomographic technique, as discussed in detail in [4], the SRT always guarantees convergence, even when increasing the number of measurement paths (i.e., the network resolution), at the expense of processing time. The same tomographic principle exploited for rainfall monitoring can be utilized for the application discussed in this paper, since the objective is the same: reconstructing 2–D fields (in this context the concentrations of molecular species), which causes the attenuation measured along some selected paths. The results presented in this paper are obtained by applying the SRT. The interested reader is thus referred to [4] for the complete and detailed description of the processing algorithm and of the reasons that led to its development. Here, we simply point out that the final estimated concentration field $\hat{c}(x, y)$ over a plane surface is expressed as a linear combination of N_{PC} 2–D Gaussian symmetrical functions, called pseudo cells (PC's)

$$\hat{c}(x, y) = \sum_{i=1}^{N_{\mathrm{PC}}} s_i \cdot h_i(x, y) \tag{26}$$

where

$$\begin{aligned} h_i(x, y) &= h(\rho_i, W_i) \\ &= \frac{1}{\sqrt{2\pi}} \exp\left(\frac{-\rho_i^2}{2W_i^2}\right)_{i=1, 2, \cdots N} \\ \rho_i &= \sqrt{(x - X_i)^2 + (y - Y_i)^2} \end{aligned} \tag{27}$$

where (X_i, Y_i) are the center coordinates of the ith PC, while W_i is the PC's width. Differently from the rainfall microwave application, the PC's Gaussian shape is not utilized for a particular physical reason, but simply because each PC is infinitely derivable, and this guarantees continuity of the reconstructed concentration field, and also because the attenuation contribution of each PC is easily computed thanks to the function's separability, thus increasing the global SRT computational speed.

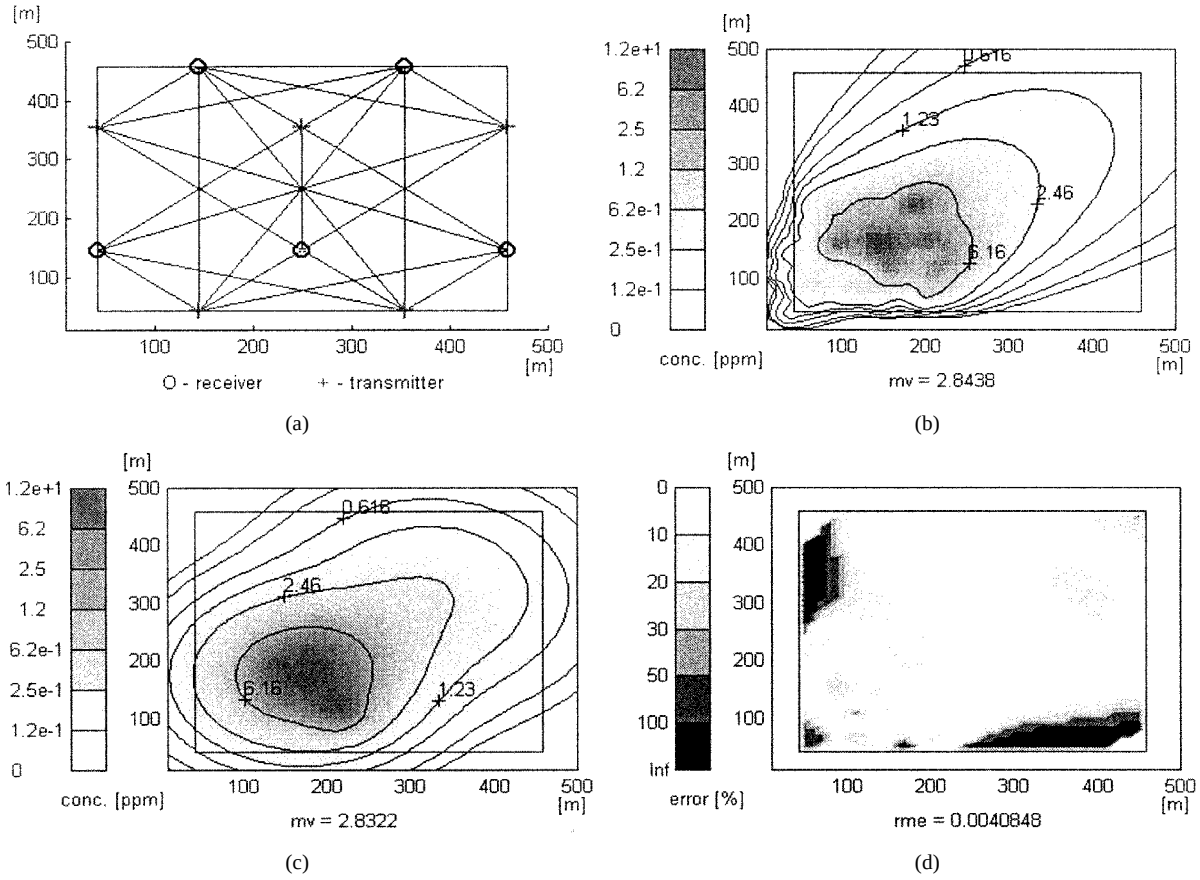

Fig. 18. Reconstruction of the simulated concentration field produced by 40 spot sources of CO randomly distributed inside a 200 × 200 m square surface. Pasquill's stability class A and NET01.

B. Simple Model for Simulating Diffusion of Pollutants

The diffusion of pollutants is a very complex phenomenon due to the high number of chemical and physical factors involved. Its modelization is therefore a very arduous task in general. In urban areas, it is even more complicated by several specific factors related to the urban pattern, to the surrounding orography, and to the location and importance of the emitting sources. Our purpose however, is simply to evaluate the performance of the tomographic algorithm. Thus, it is sufficient to adopt simplified diffusion models, through which it is possible to generate concentration fields $c(x, y)$ having a dynamic range of variation across the x–y plane (at a given instant) that is in good agreement with experimentally measured point values. On the other hand, notice that the reconstruction performance of the tomographic inversion algorithm, for a given topology of the measurement network, depends mainly on the spatial detail of the original field and not on its 2–D pattern. In other words, the measurement network heavily conditions the spatial resolution of the reconstructed field $\hat{c}(x, y)$.

The model we adopted is the Gaussian Slender Plume model [16]. It gives the mean value at regime of the concentration of a gaseous substance introduced in the atmosphere by a point source placed in $(x, y, z) = (0, 0, h)$

$$\langle c(r)\rangle = \frac{q}{2\pi u\sigma_y\sigma_z} e^{-(y^2/2\sigma_y^2)} \cdot \left[e^{-((z-h)^2/2\sigma_z^2)} + e^{-((z+h)^2/2\sigma_z^2)}\right] \quad (28)$$

where $r = \sqrt{x^2+y^2+z^2}$, with z being the altitude; q is the amplitude of the source (in g/s); u is the wind speed along the x direction; and σ_y, σ_z are the dispersion parameters along the y and z directions, respectively, accounting for atmospheric conditions in terms of turbulence.

The Gaussian Slender Plume model is valid under the following restrictive conditions [16]:

stationary wind;
negligible diffusion effects along the wind direction;
homogeneous and stationary turbulence conditions;
completely reflecting terrain (no absorption by the terrain).

The model was used by accounting for the analytical expressions derived for each dispersion parameter $\sigma_y e \sigma_z$ in correspondence with each of the six Pasquill's stability classes [16]:

1) extremely unstable;
2) moderately unstable;
3) slightly unstable;
4) neutral;
5) slightly stable;
6) moderately stable.

Consistently with the simple diffusion model adopted, the gaseous substance considered for simulations is the carbon monoxide. In fact, the CO pollution sources (e.g. heating and internal combustion engines), can be reasonably assimilated to point sources. Average concentrations along each measurement link were obtained through 2-D sampling of the simulated

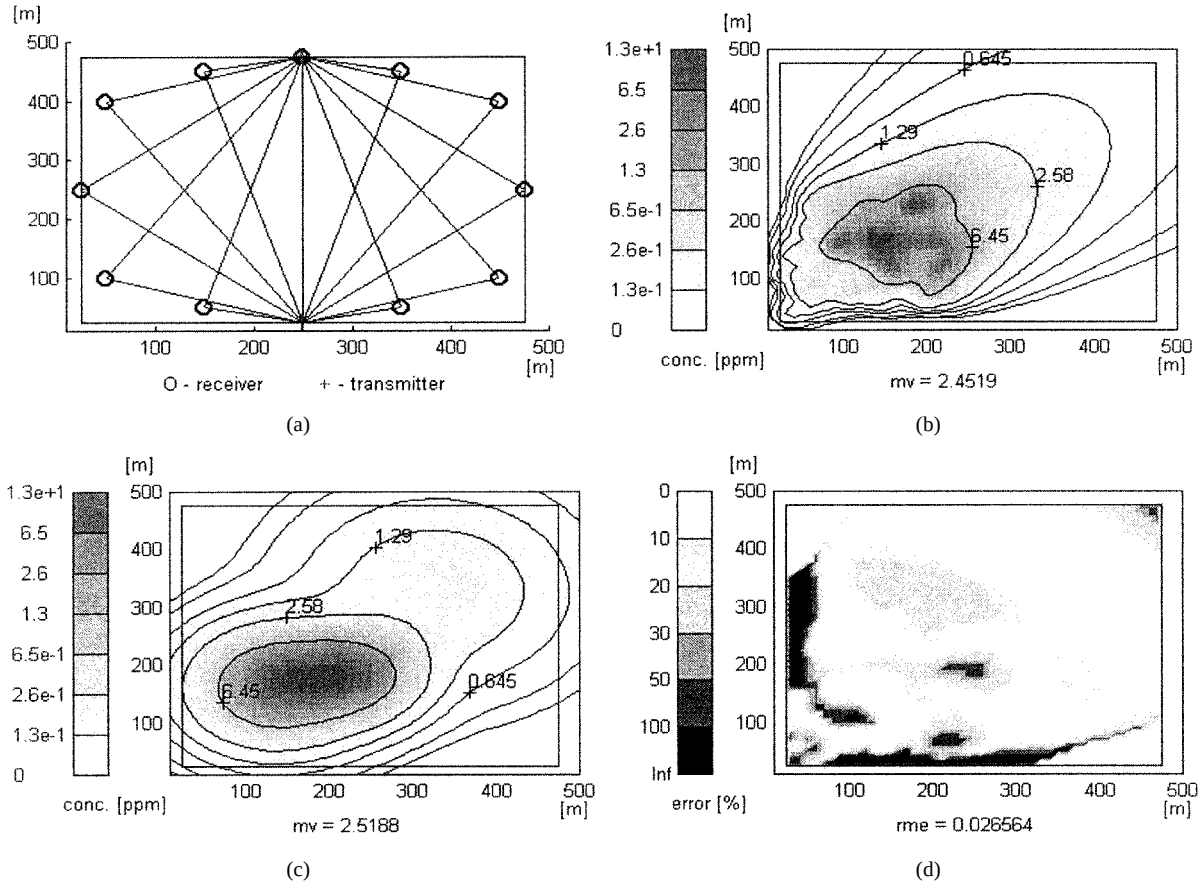

Fig. 19. As Fig. 18, for NET02.

concentration fields and following bilinear interpolation, according to the topology of the adopted measurement network.

In the following, we show the performance of the proposed tomographic system in some representative cases, in particular, the ability of the SRT algorithm to retrieve with very good accuracy the average concentration of the specific pollutants over the monitored area and to reconstruct the 2-D pattern of the concentration field of the pollutants.

C. Adopted Network Topologies

The tomographic inversion algorithm was applied utilizing the two measurement networks (called "NET01" and "NET02") reported in Figs. 12 and 13.

The NET01 network consists of five transmitter–receiver pairs and five retroreflectors. NET01 provides a good coverage of the 2-D fields to be monitored, jointly with a quite good intrinsic spatial resolution. Instead, the NET02 network consists of only two transmitter–receiver pairs and 12 retroreflectors. It is designed to minimize the number of transmitter–receiver pairs and consequently, the cost of the entire network. The cost of a transmitter–receiver pair is in fact remarkably higher than that of a retroreflector. Compared to NET01, NET02 has an intrinsically lower spatial resolution capability.

Notice that in addition to the problem of the global cost of the network, the processing time required by the tomographic algorithm must be considered, too. An increase of the network complexity in terms of number of links and links crosses causes an increase of processing time. NET01 and NET02 require, respectively, seven and three minutes on average on a standard Pentium 100 MHz personal computer to make one reconstruction.

D. Performance of the Tomographic Reconstruction

The first CO concentration field $c(x, y, z)$ considered in simulations is generated by one point source located in $(x_o, y_o, z_o) = (20, 100, 0.5)$ m. We assumed a source amplitude of 1 g/s (quantitatively equivalent to the emission of a few internal combustion engines), 0.3 m/s horizontal wind, and an atmosphere in Pasquill's stability class A for the aforementioned dispersion parameters.

The simulated tomographic reconstruction was performed at an altitude of 5 m, and over a square surface with a 200 m side (x and y range between 0–200). Fig. 14 and Fig. 15 refer to NET01 and NET02, respectively. The reconstruction error is evaluated through relative mean error (RME) (the relative error between mean values) and the distribution of the relative error. The latter is reported in the bottom-right frames of each figure. The error has been computed over the rectangular area (plotted in frames (b), (c), and (d) of each figure). Such area strictly depends on the measurement network, since it is the minimum rectangular area that contains all measurement links.

The second simulated CO field is generated by one point source like the first one, but it is located in $(x_o, y_o, z_o) = (20, 20, 0.5)$ m, with a wind of 5 m/s blowing in the northeast

direction and the atmosphere as in Pasquill's stability class D. The resulting reconstruction is reported in Figs. 16 and 17, structured like the two previous figures. This combination of point source, wind, and stability class generates fields characterized by high spatial variation, of interest to test the performance of the reconstruction algorithm in such conditions.

The third simulation still concerns a CO concentration field. It refers to 40 point sources randomly located in a 200×200 m square surface, 0.5 m above the ground, with uniform probability density. The amplitude of each source ranges between 0.1 and 0.5 g/s. As before, we considered an unstable atmosphere with a horizontal 0.3 m/s wind speed. In this case, the concentration field was analyzed over a square surface with a 500 m side, located 5 m above the ground. The results of reconstructions for both measurement networks are reported in Figs. 18 and 19.

Note that the relative error reported in frame (d) is computed only where both the simulated and reconstructed concentration fields exceed 1/1000 of the respective maximum values. This avoids misleading interpretations of errors that would be due only to high relative variations at nonsignificant concentration levels. Both NET01 and NET02 were able to reconstruct the three given concentration fields with quite small RME values. Notice also that the spatial pattern is caught by the networks with appreciable fidelity, as shown by frame (d) of Figs. 16–19.

VIII. Conclusions

The investigations described in this work gave positive indications about the feasibility and performance of the proposed tomographic system based on infrared attenuation measurements for the observation of the 2-D distribution of air pollutants over limited areas.

The reported results should be evaluated in the light of the following remarks, which lead us to expect a still better performance.

1) A very restrictive assumption has been made concerning the cumulative attenuation of atmospheric components. In fact, we referred to their maximum observed concentration in order to establish the maximum affordable extent of the monitored area. Actually, that extent could be significantly larger.
2) The number of transmitters and receivers employed in the network can be reduced if they are positioned on a step revolving platform, in order to activate transmission links also over adjacent areas.
3) An improved reconstruction of the pollution concentration field can be expected by exploiting time-correlation of the subsequent observed fields (this type of improvement has been proposed and evaluated for an analogous microwave tomographic system for monitoring rainfall fields [4]).
4) The used network topologies are not necessarily optimum. From the application point of view, issues 5–8 are worth highlighting.
5) Near-ground concentration field monitoring through the proposed system can be operated only in very particular areas that are obstacle-free along the transmission paths.
6) More typically, the proposed system can be used for monitoring horizontal concentration fields at a height of a few tenths meters (especially in urban areas).
7) With respect to current systems, which are based on spot sensors distributed in the area to be monitored and often provide measurements excessively affected by local anomalies, the proposed tomographic system appears instead capable of providing a more robust and resolved estimate of the horizontal concentration field.
8) It is envisaged that the proposed tomographic system can provide more robust synthetic indices of air pollution, as needed to manage the related risk in inhabited areas.

Concerning points 1 and 2, it is expected that the dynamics of the concentration field (even at some tenths meters of height), as observable through time continuos monitoring of the target area by the proposed tomographic system, can be exploited to predict the concentration field near ground, as well as for better prediction and management.

Acknowledgment

The authors wish to thank D. Joseph, Data Support Section, NCAR/SCD, Boulder, CO, for his help.

References

[1] R. T. Ku, E. D. Hinkley, and J. O. Sample, "Long-path monitoring of atmospheric carbon monoxide with a tunable diode laser system," *Appl. Opt.*, vol. 14, no. 4, pp. 854–861, 1975.
[2] D. T. Cassidy and J. Reid, "Atmospheric pressure monitoring of trace gases using tunable diode lasers," *Appl. Opt.*, vol. 21, no. 7, pp. 1185–1190, 1982.
[3] D. Giuli, A. Toccafondi, G. Biffi Gentili, and A. Freni, "Tomographic reconstruction of rainfall fields through microwave attenuation measurements," *J. Appl. Meteorol.*, vol. 30, pp. 1323–1340, 1991.
[4] D. Giuli, L. Facheris, and S. Tanelli, "Microwave tomographic inversion technique based on a stochastic approach for rainfall fields monitoring," *IEEE Trans. Geosci. Remote Sensing*, vol. 37, pp. 2536–2555, Sept. 1999.
[5] E. D. Hinkley, "Laser Monitoring of the Atmosphere," in *Topics in Applied Physics*. New York: Springer-Verlag, 1976.
[6] L. S. Rothman, "AFGL trace gas compilation: 1982 version," *Appl. Opt.*, vol. 22, no. 11, pp. 1616–1625.
[7] ——, "The HITRAN database: 1986 edition," *Appl. Opt.*, vol. 26, pp. 4058–4097, 1987.
[8] R. M. Measures, *Laser Remote Sensing*: Wiley, 1981.
[9] W. Demtroeder, *Laser Spectroscopy*. New York: Springer Verlag, 1981.
[10] P. Werle, "A review of recent advances in semiconductor laser based gas monitors," *Spectrochimica Acta*, vol. 54, pp. 197–236, 1998.
[11] V. E. Zuev, *Propagation of Visible and Infrared Radiation in the Atmosphere*. New York: Springer Verlag.
[12] A. Ishimaru, *Wave Propagation and Scattering in Random Media*. New York: Academic, 1978.
[13] H. Beaumont, "Caractérization de la turbolence atmosphérique et procédure déamélioration des images pour des observations horizontales au dessus de la mer," Ph.D. dissertation, Dépt. Astrophys., Univ. Nice-Sophia Antipolis, France, 1996.
[14] E. D. Hinkley, K. W. Nill, and F. A. Blum, "Laser spectroscopy of atoms and molecules," *Topics Appl. Phys.*, vol. 2, 1976.
[15] P. W. Kruse, L. D. Mc Glauchin, and R. B. Mc Quistan, *Elements of Infrared Technology*. New York: Wiley, 1963.
[16] J. H. Seinfeld, *Atmospheric Chemistry and Physics of Air Pollution*. New York: Wiley, 1986.

Fabrizio Cuccoli received the Laurea degree (cum laude) in electronic engineering from the University of Florence, Italy, in 1996. Since 1997, he has been a Ph.D. student in methods and technologies for environmental monitoring.

He is presently with the Radar and Radiocommunications Laboratory Group, Department of Electronic Engineering, University of Florence. His main research activity is in the area of remote sensing of rainfall and of the atmosphere through active and passive systems (e.g., spaceborne rain radars, and infrared and microwave Earth–satellite links). His current interest is the microwave and infrared spectral analysis of absorption characteristics of the atmosphere components and related attenuation measurements data processing.

Luca Facheris received the Laurea degree (cum laude) in electronic engineering from the University of Florence, Italy, in 1989. He received the Ph.D. degree in electronic and information engineering in 1993 from the University of Padua, Italy.

Since 1993, he has served as an Assistant Professor in the telecommunications area, Department of Electronic Engineering, University of Florence. His main research activity is in the area of signal and data processing for active remote sensing, with particular reference to radar polarimetry and ground and spaceborne weather radars.

Simone Tanelli (S'94) received the Laurea degree (cum laude) in electronic engineering from the University of Florence, Italy, in 1995.

Since 1995, he has been a Ph.D. student in methods and technologies for environmental monitoring. He is presently with the Radar and Radiocommunications Laboratory Group, Department of Electronic Engineering, University of Florence. His main research activity is in the area of remote sensing of atmosphere. In particular, his research interests include tomographic inversion problems, spectral analysis of absorption measurements through atmosphere, and weather radar data processing.

Dino Giuli (SM'84) received the Laurea degree (cum laude) in electronics engineering from the University of Pisa, Italy, in 1970.

Since 1973, he has been a Faculty Member, Department of Electronics, University of Florence, Italy, where he serves now as Full Professor. His research activity has mainly been devoted to experimental and theoretical research in the field of radar systems. He is also involved in research in digital communications and telecommunication networks. His current radar research is devoted to optimum processing of dual-polarization radar signals and data and to their integration with data from other spacebome or ground-based sensors.

Prof. Giuli is a member of the Italian Electrical Association (AEI).